Cooperative tin oxide fullerene electron selective layers for high-performance planar perovskite solar cells†

Weijun Ke,[abc] Dewei Zhao,[a] Chuanxiao Xiao,[c] Changlei Wang,[a] Alexander J. Cimaroli,[a] Corey R. Grice,[a] Mengjin Yang,[c] Zhen Li,[c] Chun-Sheng Jiang,[c] Mowafak Al-Jassim,[c] Kai Zhu,[c] Mercouri G. Kanatzidis,[d] Guojia Fang*[b] and Yanfa Yan*[a]

[a]*Department of Physics and Astronomy and Wright Center for Photovoltaics Innovation and Commercialization, The University of Toledo, Toledo, OH 43606, USA. E-mail: yanfa.yan@utoledo.edu*
[b]*Key Laboratory of Artificial Micro- and Nano-structures of Ministry of Education of China, School of Physics and Technology, Wuhan University, Wuhan 430072, China. E-mail: gjfang@whu.edu.cn*
[c]*National Renewable Energy Laboratory, 15013 Denver West Parkway, Golden, CO 80401, USA*
[d]*Department of Chemistry, Northwestern University, Evanston, IL 60208, USA*

†Electronic supplementary information (ESI) available. See DOI: 10.1039/x0xx00000x

Abstract

Both tin oxide (SnO_2) and fullerenes have been reported as electron selective layers (ESLs) for producing efficient lead halide perovskite solar cells. Here, we report that SnO_2 and fullerenes can work cooperatively to further boost the performance of perovskite solar cells. We find that fullerene can be redissolved during perovskite deposition, allowing ultra-thin fullerene to be retained at the interface and some dissolved fullerenes infiltrate into perovskite grain boundaries. The SnO_2 layer blocks holes effectively; whereas, the fullerenes promote electron transfer and passivate both the SnO_2/perovskite interface and perovskite grain boundaries. With careful device optimization, the best-performing planar perovskite solar cell using a fullerene passivated SnO_2 ESL has achieved a steady-state efficiency of 17.75% and a power conversion efficiency of 19.12% with an open circuit voltage of 1.12 V, a short-circuit current density of 22.61 mA cm^{-2}, and a fill factor of 75.8% when measured under

reverse voltage scanning. We find that the partial dissolving of fullerenes during perovskite deposition is the key for fabricating high-performance perovskite solar cells based on metal oxide/fullerene ESLs.

1. Introduction

Organic-inorganic lead halide perovskite solar cells have attracted significant attention recently due to their excellent photovoltaic properties, such as an extremely high optical absorption coefficient, very long carrier lifetime and tunable band gap.[1-9] The power conversion efficiency (PCE) of perovskite solar cells has rapidly increased from 3.8% to 22.1%.[10-21] High efficiency perovskite solar cells exclusively use electron selective layers (ESLs), which transport electrons but block holes, and hole selective layers (HSLs), which transfer holes but block electrons.[22-24] To perform adequately in this manner, the ESLs and HSLs should not be heavily doped. Therefore ESLs and HSLs must be thin and compact to avoid high series resistance and shunting. High quality ESLs and HSLs are essential for obtaining photovoltaic devices with high short-circuit current densities (J_{sc}), open-circuit voltages (V_{oc}), and fill factors (FF).[22, 23] For perovskite solar cells with a regular structure, metal oxides, such as TiO_2 and ZnO, have been reported as excellent ESL materials.[16, 19, 25-28] Recently, SnO_2 has been reported as an alternative ESL material for high efficiency perovskite solar cells.[29-36] It has been shown that low-temperature compact SnO_2 films exhibit good antireflection behavior, good band edge alignment with perovskite absorbers, and high electron mobility.[29, 31] Despite the aforementioned advantages, metal oxide ESL/perovskite interfaces have not yet reached their full potential. It has been demonstrated that enhancing the charge transfer and

reducing the interface recombination can effectively improve the performance of perovskite solar cells.[37-39] Fullerenes, such as C_{60} and phenyl-C_{61}-butyric acid methyl ester (PCBM), are excellent acceptors in organic solar cells.[40, 41] They have also been reported as good ESL materials for perovskite solar cells.[42-48] It has been shown that fullerenes effectively promote charge transfer and passivation of perovskites.[49-51] However, fullerene ESLs cannot block holes as efficiently as metal oxide ESLs due to their relatively smaller band gaps. It is therefore prudent to combine metal oxide ESLs with fullerenes to harness the benefits of each while avoiding their shortfalls. If they are able to work cooperatively, i.e., the metal oxide layer effectively block holes and the fullerenes promote electron transfer and passivation of the perovskite layer, the metal oxide/fullerene ESLs may further boost the performance of perovskite solar cells. Some groups have tried metal oxide/fullerene combinations and moderate improvements on cell performance have been achieved.[52-58] However, so far, the role of fullerene has not been clarified clearly.

In this paper, we show that the fullerene can be redissolved by DMF and DMSO during spin-coating of the perovskite precursor, which allows only ultra-thin fullerene to be retained at the interface and some dissolved fullerenes infiltrate into perovskite grain boundaries. Therefore, the ultra-thin fullerene effectively passivate both the ESL/perovskite interface and perovskite grain boundaries. The use of ultra-thin PCBM does not adversely affect the *J*sc of perovskite solar cells, which is critical for realizing high PCEs. The roles of fullerenes are confirmed by photoluminescence (PL), time-resolved photoluminescence (TRPL), and Electrochemical impedance spectroscopy (EIS) measurements, revealing that the cells using SnO_2/PCBM ESLs exhibit

enhanced electron transfer and reduced interface recombination than the cells using SnO_2-only ESLs. Furthermore, the conductive atomic-force microscopy (c-AFM) results also show that PCBM passivates the perovskite grain boundaries and reduce the dark current. We show that SnO_2 and ultra-thin fullerene films can work cooperatively to significantly boost the performance of perovskite solar cells as compared to the cells solely using SnO_2 ESLs. With careful optimization of the PCBM passivated SnO_2 (name SnO_2/PCBM hereafter) ESLs and perovskite layers, our best-performing perovskite solar cell achieved a steady-state efficiency of 17.75% and a PCE of 19.12% with a high J_{sc} of 22.61 mA cm^{-2}, V_{oc} of 1.12 V, and FF of 75.83% when measured under reverse voltage scanning. The average PCE of the 30 cells using SnO_2/PCBM ESLs is 17.88 ± 0.48%, whereas, the average PCE of the 30 separate cells using SnO_2-only ESLs is 16.50 ± 0.40%. Our results confirm that the combined SnO_2/ultra-thin PCBM ESL is an excellent candidate for fabricating high-efficiency perovskite solar cells.

2. Experimental section

Device fabrication

SnO_2 ESLs were prepared by a low-temperature solution process described in our previous work.[29] 0.1 mol/L $SnCl_2$ (Alfa, anhydrous 99.9985%) was dissolved in ethanol and spin-coated on clean fluorine-doped SnO_2 (FTO) substrates in atmosphere (TEC 15, Hartford Glass Co) with a spin condition of 500 rpm for 1s and then 2000 rpm for 30s. The films were subsequently annealed on a hotplate in atmosphere with a three-step annealing process: 100°C for 1 h, 150°C for 1 h and finally 185°C for 1 h. The thickness of the SnO_2 ESL is roughly 40 nm. SnO_2/PCBM ESLs were prepared by spin-coating

PCBM dichlorobenzene solutions on SnO_2 films with a spin rate of 2000 rpm for 30 s and then annealed on a hotplate at 100 °C for 10 min in a glove box. The thickness of the PCBM films was controlled by adjusting the concentration of PCBM in dichlorobenzene. A 5 nm thick C_{60} (Luminescence Technology Co., Ltd, >99.5%) film was deposited on a SnO_2 film by thermal evaporation at a rate of 0.02 nm/s.[44] Compact perovskite absorber layers were deposited on the ESLs by using a solvent engineering method reported in the literature.[59] The perovskite films were prepared by spin-coating the precursor solution consisting of 461 mg PbI_2 and 159 mg CH_3NH_3I dissolved in 723 μL N,N-dimethylformamide and 81 μL dimethyl sulfoxide. The molar ratio between PbI_2 and CH_3NH_3I is 1:1. The perovskite films were annealed at 60°C for 2 min and then 100°C for 5 min in a glovebox. The solution of HSLs consisted of 72.3 mg 2,2',7,7'-tetrakis-(N,N-di-p-methoxyphenylamine)-9,9'-spirobifluorene (spiro-OMeTAD) (Shenzhen Feiming Science and Technology Co., Ltd., 99.0%), 17.5 μL Li-bis-(trifluoromethanesulfonyl) imide (LiTFSI) (Sigma, 99.95%) (520 mg/mL in acetonitrile), 28.8 μL 4-tert-butylpyridine (TBP) (Sigma, 96%), and 28.9 μL FK 102 Co(III) TFSI Salt (300 mg/mL in acetonitrile) (Dyesol) in 1 mL chlorobenzene (Sigma, 99.8%). The solution of HSLs was stirred for 12 h and then coated on the perovskite films at 500 rpm for 1 s and finally 2000 rpm for 60 s in a dry box. To complete the devices, 60 nm thick Au electrodes were thermally evaporated on top of the HSLs. The active area of the cells was 0.08 cm^2.

Film and device characterization

The morphology of the devices and the perovskite films were characterized by a high-resolution field emission scanning electron microscopy (SEM) (Hitachi S-4800). Atomic-force microscopy (AFM) and conductive atomic-force microscopy c-AFM was performed on a Veeco D5000 AFM in glovebox equipped with the Nanoscope V controller. A nanosensor PPP-EFM tip was used in contact mode for the measurement. The crystallinity of perovskite films was examined by X-ray diffraction (XRD) (Rigaku Ultima III) with a Cu Kα radiation source with the operation conditions of 40 kV and 44 mA. Ultraviolet–visible (UV-vis) absorbance and transmission spectra were measured by an UV-vis spectrophotometer (PerkinElmer Lambda 1050). External quantum efficiency (EQE) spectra were taken on a QE system (PV Measurements Inc.). Photocurrent density-voltage (*J-V*) curves were measured by a Keithley Model 2400 under AM1.5G simulated irradiation with a standard solar simulator (PV Measurements Inc.) and a voltage settling time of 10 ms. The light intensity of the solar simulator was calibrated by a standard silicon solar cell. EIS measurements were performed on an electrochemical workstation (Voltalab PGZ-301) at a bias voltage of 0 V in the dark.

3. Results and discussion

The solar cells fabricated in this study have the regular cell structure using either SnO_2 or SnO_2/PCBM ESLs, shown in Fig. S1a†. The PCBM is deposited between the perovskite film and the SnO_2 film. The HSL material is spiro-OMeTAD. The charge separation process of the photo-generated carriers is shown in Fig S1b†. The ESL and HSL have band edges matching well with that of the perovskite absorber: suitable for carrier separation and transportation. The processes for depositing the perovskite layers, spiro-OMeTAD HSLs, and back electrodes were identical for cells fabricated

with different ESLs. Fig. 1a shows the *J-V* curves of two representative planar perovskite solar cells using SnO_2 and SnO_2/PCBM ESLs. The solar cell using an unpassivated SnO_2 ESL achieved a PCE of 16.53% with a V_{oc} of 1.09 V, a J_{sc} of 21.13 mA cm^{-2}, and an FF of 71.49% when measured under reverse voltage scanning. The solar cell using a SnO_2/PCBM ESL achieved a PCE of 18.17% with a V_{oc} of 1.11 V, a J_{sc} of 21.41 mA cm^{-2}, and an FF of 76.20% when measured under reverse voltage scanning. The PCBM layer was deposited by spin-coating a 10 mg/mL PCBM in dichlorobenzene precursor on the SnO_2 film. The solar cells using the SnO_2/PCBM ESLs exhibited significant improvements of all photovoltaic parameters, V_{oc}, J_{sc}, FF, and PCE, as compared to solar cells using solely SnO_2 ESLs. The V_{oc} increased from 1.09 V to 1.11 V, J_{sc} increased from 21.13 mA cm^{-2} to 21.41 mA cm^{-2}, and the FF increased from 71.49% to 76.20%, and therefore, the PCE increased from 16.53% to 18.17%. When measuring the *J-V* curves of these solar cells under the forward scanning condition, as shown in Fig. 1a, both types of cells exhibited hysteretic *J-V* behavior.[60-62] The solar cell using a SnO_2 ESL showed a PCE of 14.91% with a V_{oc} of 1.04 V, a J_{sc} of 21.10 mA cm^{-2}, and an FF of 67.77% when measured under forward voltage scanning. The solar cell using a SnO_2/PCBM ESL showed a PCE of 16.91% with a V_{oc} of 1.08 V, a J_{sc} of 21.42 mA cm^{-2}, and an FF of 73.01% when measured under forward voltage scanning. The photovoltaic parameters measured under different voltage scan directions are summarized in Table 1. It is obvious that the performance of the solar cell using the SnO_2/PCBM ESL is much better than that of the solar cell using the SnO_2 ESL. Fig. 1b shows the measured EQE spectra of the cells using SnO_2 and SnO_2/PCBM ESLs. The integrated current densities based on these curves are 20.34 and 20.67 mA cm^{-2} for the cells using the SnO_2 ESL and SnO_2/PCBM ESL, respectively, which are close to the J_{sc}'s obtained from the *J-V*

measurements. Solar cells using only PCBM as the ESL showed much lower performance. Figure S2 shows the UV-vis absorbance spectrum, *J-V* curves, and EQE spectrum of the solar cell using only PCBM ESL without SnO_2. The perovskite film deposited on PCBM-coated FTO substrate has a similar absorption as those deposited on SnO2/PCBM-coated substrates. However, the solar cell using only PCBM ESL showed a PCE of 14.60% (10.57%) with a V_{oc} of 1.03 V (0.85 V), a J_{sc} of 20.37 mA cm^{-2} (20.24 mA cm^{-2}), and an FF of 69.44% (61.57%) when measured under reverse (forward) voltage scanning. Therefore, it is important to cooperate SnO_2 with PCBM as the ESLs to achieve higher performance.

The efficiency enhancement from the use of SnO_2/PCBM ESLs is verified by the averaged efficiency of 30 separate cells using SnO_2 ESLs and 30 separate cells using SnO_2/PCBM ESLs. Fig. 1c displays a histogram of the PCEs of these cells measured under reverse voltage scanning. It demonstrates good reproducibility of our fabricated solar cells. The average V_{oc}, J_{sc}, FF, and PCE for the 30 cells using SnO_2/PCBM ESLs are 1.11 ± 0.01 V, 21.21 ± 0.64 mA cm^{-2}, 76.19 ± 1.17%, and 17.88 ± 0.48%, respectively. However, the average V_{oc}, J_{sc}, FF, and PCE for the 30 separate cells using SnO_2 ESLs without PCBM are 1.07 ± 0.02 V, 20.82 ± 0.29 mA cm^{-2}, 74.23 ± 1.90%, and 16.50 ± 0.40%, respectively. It is evident that the use of SnO_2/PCBM ESLs can improve all photovoltaic device performance parameters, including efficiency. We also measured the steady-state efficiency of cells using both SnO_2/PCBM and unpassivated SnO_2 ESLs by applying constant bias voltages that are consistent with the measured maximum power points in *J-V* measurements. The steady-state efficiency of the two solar cells, whose *J-V* curves are shown in Fig. 1a, are shown in Fig. 1d. The current densities first increased and then

stabilized after applying a constant bias. The steady-state efficiencies of the cells using the SnO_2 and SnO_2/PCBM ESLs are 15.51% and 17.28%, respectively. These values are very close to the values averaged from the efficiencies obtained from the *J-V* curves measured under different voltage scanning directions. Just like the photovoltaic performance obtained from the *J-V* curves, the steady-state efficiency of the cell using a SnO_2/PCBM ESL is much higher than that of the cell using only SnO_2 as the ESL. It is also noted that the steady-state efficiency reaches the maximum value much faster for the cell using a SnO_2/PCBM ESL than for the cell using an unpassivated SnO_2 ESL. This indicates that SnO_2/PCBM ESL promotes electron transfer and reduces interface recombination.

Structural characterization reveals that the use of different ESLs did not cause any obvious changes to the grain size, thickness, or crystallinity of the perovskite layer, indicating that the performance enhancement induced by the use of the SnO_2/PCBM ESL is likely due to the improvement of the ESL/perovskite interface. Fig. 2a, b show the top view SEM images of the perovskite films grown on the SnO_2 ESL and SnO_2/PCBM ESL, respectively. The perovskite films deposited on these two ESLs showed very similar surface morphology. Both films are uniform, compact, and have no obvious pin holes. The grain sizes are about 500 nm. Fig. 2c, d show cross-sectional SEM images of the cells using SnO_2 and SnO_2/PCBM ESLs, respectively. The perovskite films have very similar thicknesses, about 600 nm. These results are consistent with conclusion from XRD patterns shown in Fig. S3†, i.e., the use of the SnO_2/PCBM ESL does not change the crystallinity of perovskite films.

Because PCBM has a band gap of ~1.8 eV, it is critical to keep the PCBM layer as thin as possible so that the incorporation of PCBM would not adversely affect the current of the cells. Because the PCBM layer can be partially dissolved by DMF and DMSO during spin-coating of the perovskite precursor, the optimal PCBM amount can be realized by controlling the concentration of the PCBM solution. Fig. S4† shows the *J-V* curves of the cells using SnO_2/PCBM ESLs with PCBM films deposited from solutions of 5, 10, and 15 mg/mL PCBM in dichlorobenzene. It shows that the PCBM solution with a concentration of 10 mg/mL yielded the best-performing cells. The photovoltaic parameters of the cells using the SnO_2/PCBM layer ESLs, with PCBM deposited by using the precursor solutions with varying PCBM concentrations, are summarized in Table S1†. Fig. 3a shows the transmission spectra of the FTO substrates covered with SnO_2 and SnO_2/PCBM ESLs. It is seen that the PCBM film prepared using a 10 mg/mL PCBM solution exhibits a strong absorption in the short wavelength range due to the absorption of PCBM. However, the perovskite films deposited on SnO_2 and SnO_2/PCBM ESLs show almost identical absorbance spectra (Fig. 3b). The perovskite film deposited on SnO_2/PCBM ESL doesn't show a PCBM absorption peak at ~689 nm, indicating that most PCBM are washed away during the spin-coating process of the perovskite precursor, and the remaining PCBM must be just enough for passivation of SnO_2. Such a thin, residual PCBM layer could not even be seen in our cross-sectional transmission electron microscopy and Fourier transform infrared spectroscopy measurements. Therefore, the residual PCBM is not expected to significantly reduce the J_{sc} and QE of the cell, as shown in Fig. 1a, b. As evidenced from the above characterizations, the use of different ESLs did

not cause any obvious change to the grain size, thickness, or crystallinity of the perovskite layers. Therefore, the performance enhancement induced by the use of a SnO_2/PCBM ESL is most likely due to the improvement of the ESL/perovskite interfacial properties, such as better electron transfer and less charge recombination.

To further study the PCBM passivation effect, PL and TRPL were measured for perovskite films grown on SnO_2 and SnO_2/PCBM ESLs. Fig. 4a shows the PL spectra of the perovskite films, which show emission peak at about 760 nm. It is seen that the PL intensity of the film deposited on SnO_2/PCBM ESL is much lower than that of the film deposited on SnO_2 ESL, while two films exhibit very similar absorption. The significantly reduced PL intensity can be attributed to the quenching effect caused by the faster electron transfer promoted by the PCBM. The TRPL results of the perovskite films deposited on SnO_2 and SnO_2/PCBM ESL are shown in Fig. 4b. The curves were fitted by a biexponential decay function, while τ_1 and τ_2 represents the bulk recombination in perovskite bulk films and the delayed recombination of trapped charges, respectively.[57] The values and ratio of $\tau 1$ and $\tau 2$ are summarized in Table S2†. It shows that the perovskite film deposited on SnO_2/PCBM ESL has a much lower $\tau 2$ with a lower ratio of $\tau 2/ \tau 1$, indicating a faster electron transfer process and lower the trap state density, as compared to the film deposited on SnO_2 ESL. Therefore, the solar cells using the SnO_2/PCBM ESLs have lower interface recombination.

As the PCBM can be dissolved in DMF during spin-coating the perovskite precursor, a small amount of PCBM infiltrate into the perovskite films and passivate perovskite gran boundaries. To confirm the passivation effects of the

PCBM, we also measured the AFM and the corresponding c-AFM images of the perovskite films deposited on SnO_2 and SnO_2/PCBM ESLs. The AFM images shown in Fig. 5a and c exhibit similar contrast, revealing similar surface morphology for these perovskites. However, the c-AFM images with an applied bias of 0.25 V shown in Fig. 5b present rather different contrast, especially at grain boundaries. There is no direct correlation between the current and AFM images, suggesting that the observed difference in GB features is not due to artificial topographic effects. Although the current route spreads out from the contact, the spreading resistance is dominated by the nm-scale volume of the sample right below the probe, resulting in nm-resolution resistivity mapping. The film deposited on SnO_2 ESL shows higher intensity, which indicates a higher local current, at grain boundaries than in grain interior. However, for the perovskite film deposited on PCBM, there are much less grain boundaries showing higher current. The average current at grain interior and grain boundaries for the film deposited on SnO_2 ESL are 21.16 and 26.63 pA, respectively. However, the average current at grain interior and grain boundaries for the film deposited on SnO_2/PCBM ESL are 12.65 and 18.25 pA, respectively. The reduced current for the sample with PCBM can be attributed to the PCBM can passivate the perovskite film and therefore can reduce the trap state density of the film.

Electrochemical impedance spectroscopy (EIS) has been widely used to investigate charge recombination and transport at the interfaces in perovskite solar cells.[63-68] To confirm that the use of a SnO_2/PCBM ESL can in fact reduce the interface charge recombination, we performed EIS measurements on cells using SnO_2 and SnO_2/PCBM ESLs. Fig. S5† shows the Nyquist plots and

equivalent circuit of the perovskite solar cells using unpassivated SnO_2 and SnO_2/PCBM ESLs. The Nyquist plots show a main semicircle in the low frequency, which is very similar to that reported the literature.[67, 68] The R_s can be assigned to the value of high-frequency intercept on the real axis. The R_{rec} in the low frequency can be assigned to the recombination between electrons and holes.[67] The R_{sc} in the high frequency can be assigned to the charge transfer at the HSL/perovskite interface, which is much lower than R_{rec}. The corresponding semicircles in the high frequency range are very small in Fig. S5†.[67, 68] The R_s, R_{sc}, and R_{rec} estimated by fitting the Nyquist plots of the perovskite solar cells using SnO_2 (SnO_2/PCBM) ESLs are 6.3 (3.4) Ω cm^2, 45.9 (42.0) Ω cm^2, and 4323.6 (40045.6) Ω cm^2, respectively. It is seen that the R_{rec} of the solar cell using the SnO_2/PCBM ESL is significantly higher than that of the cell using the SnO_2 ESL. The results indicate that the cell using the SnO_2/PCBM ESL has a much lower interface recombination rate than the cell using the SnO_2 ESL. This is in full agreement with the fact that fullerenes can significantly promote electron transfer and passivate the perovskite absorber layer. Due to the improved electron transfer and reduced charge recombination, the perovskite solar cells using SnO_2/PCBM ESLs showed improved V_{oc}'s, J_{sc}'s, FFs, and therefore PCEs as compared to the cells using SnO_2 ESLs.

Fig. 6a shows the best-performing planar perovskite solar cell using the optimized SnO_2/PCBM ESL. This cell achieved a PCE of 19.12% with a V_{oc} of 1.12 V, a J_{sc} of 22.61 mA cm^{-2}, and an FF of 75.83% when measured under reverse voltage scanning and a PCE of 18.10% with a V_{oc} of 1.11 V, a J_{sc} of 22.69 mA cm^{-2}, and an FF of 71.60% when measured under forward voltage scanning. The best-performing cell also achieved a steady-state efficiency of

17.75% with a steady-state current density of 19.48 mA cm^{-2} at a constant bias voltage of 0.911 V (Fig. 6b). It is noted that the full potential of the SnO_2/PCBM ESL has not yet been attained. If the quality of our perovskite films (e.g. grain size) can be further improved, cells with even higher efficiencies could be produced with the aid of a SnO_2/PCBM ESL.

It has been reported that, aside from PCBM, other fullerenes such as C_{60} can also promote electron transfer and reduce charge recombination. We have, therefore, fabricated the planar perovskite solar cells using SnO_2/C_{60} ESLs. Our previous work has shown that ultra-thin C_{60} can function well as an ESL and exhibits a significant passivation effect at the perovskite interface.[44, 45] Fig. S6† shows the *J-V* curve of a planar perovskite solar cell using a C_{60} passivated SnO_2 ESL. The C_{60} layer is about 5 nm thick. The solar cell achieved a PCE of 17.70% with a V_{oc} of 1.10 V, a J_{sc} of 21.21 mA cm^{-2}, and an FF of 75.55% when measured under reverse voltage scanning. Just like the SnO_2/PCBM ESL, the SnO_2/C_{60} ESL can also improve the device's overall performance.

4. Conclusions

In summary, we have shown that SnO_2 and fullerenes can work cooperatively to significantly boost the efficiency of planar perovskite solar cells. The best-performing perovskite solar cell using a PCBM-passivated SnO_2 ESL has achieved a steady-state efficiency of 17.75% and a PCE of 19.12% with a V_{oc} of 1.12 V, a J_{sc} of 22.61 mA cm^{-2}, and an FF of 75.83% when measured under reverse voltage scanning. Statistical results showed that the cells using PCBM-passivated SnO_2 ESLs yielded much better performance than the cells using unpassivated SnO_2 ESLs. Thin film and device characterizations revealed that the boost of efficiency by the use of PCBM-passivated SnO_2 ESLs is

mainly attributed to the improved electron transfer and reduced charge recombination at the ESL/perovskite interface. Our results demonstrate the potential of PCBM-passivated SnO_2 ESLs for fabricating high-efficiency planar perovskite solar cells.

Acknowledgements

This work was funded in part by the U.S. Department of Energy (DOE) SunShot Initiative under the Next Generation Photovoltaics 3 program (DE-FOA-0000990) and the Ohio Research Scholar Program. W.J.K. and G.J.F acknowledge the support from the National High Technology Research and Development Program (2015AA050601), the National Natural Science Foundation of China (61376013, 91433203, J1210061). M.J.Y. and Z.L. and K.Z. acknowledge the support from the U.S. Department of Energy under Contract No. DE-AC36-08-GO28308.

Notes and references

1. C. R. Kagan, *Science*, 1999, **286**, 945-947.
2. D. B. Mitzi, S. Wang, C. A. Feild, C. A. Chess and A. M. Guloy, *Science*, 1995, **267**, 1473-1476.
3. D. B. Mitzi, *Prog. Inorg. Chem.*, 1999, **48**, 1-121.
4. S. D. Stranks, G. E. Eperon, G. Grancini, C. Menelaou, M. J. Alcocer, T. Leijtens, L. M. Herz, A. Petrozza and H. J. Snaith, *Science*, 2013, **342**, 341-344.
5. Q. Dong, Y. Fang, Y. Shao, P. Mulligan, J. Qiu, L. Cao and J. Huang, *Science*, 2015, **347**, 967-970.
6. B. Wang, X. Xiao and T. Chen, *Nanoscale*, 2014, **6**, 12287-12297.

7. W. J. Yin, T. Shi and Y. Yan, *Adv. Mater.*, 2014, **26**, 4653-4658.

8. W.-J. Yin, T. Shi and Y. Yan, *Appl. Phys. Lett.*, 2014, **104**, 063903.

9. G. Xing, N. Mathews, S. Sun, S. S. Lim, Y. M. Lam, M. Gratzel, S. Mhaisalkar and T. C. Sum, *Science*, 2013, **342**, 344-347.

10. A. Kojima, K. Teshima, Y. Shirai and T. Miyasaka, *J. Am. Chem. Soc.*, 2009, **131**, 6050-6051.

11. J. H. Im, C. R. Lee, J. W. Lee, S. W. Park and N. G. Park, *Nanoscale*, 2011, **3**, 4088-4093.

12. H. S. Kim, C. R. Lee, J. H. Im, K. B. Lee, T. Moehl, A. Marchioro, S. J. Moon, R. Humphry-Baker, J. H. Yum, J. E. Moser, M. Gratzel and N. G. Park, *Sci. Rep.*, 2012, **2**, 591.

13. M. M. Lee, J. Teuscher, T. Miyasaka, T. N. Murakami and H. J. Snaith, *Science*, 2012, **338**, 643-647.

14. J. Burschka, N. Pellet, S. J. Moon, R. Humphry-Baker, P. Gao, M. K. Nazeeruddin and M. Gratzel, *Nature*, 2013, **499**, 316-319.

15. M. Liu, M. B. Johnston and H. J. Snaith, *Nature*, 2013, **501**, 395-398.

16. H. Zhou, Q. Chen, G. Li, S. Luo, T. B. Song, H. S. Duan, Z. Hong, J. You, Y. Liu and Y. Yang, *Science*, 2014, **345**, 542-546.

17. W. Nie, H. Tsai, R. Asadpour, J.-C. Blancon, A. J. Neukirch, G. Gupta, J. J. Crochet, M. Chhowalla, S. Tretiak and M. A. Alam, *Science*, 2015, **347**, 522-525.

18. W. S. Yang, J. H. Noh, N. J. Jeon, Y. C. Kim, S. Ryu, J. Seo and S. I. Seok, *Science*, 2015, **348**, 1234-1237.

19. N. J. Jeon, J. H. Noh, W. S. Yang, Y. C. Kim, S. Ryu, J. Seo and S. I. Seok, *Nature*, 2015, **517**, 476-480.

20. W. Chen, Y. Wu, Y. Yue, J. Liu, W. Zhang, X. Yang, H. Chen, E. Bi, I. Ashraful, M. Grätzel and L. Han, *Science*, 2015, **350**, 944-948.

21. National Renewable Energy Laboratory. Best Research-Cell Efficiencies, www.nrel.gov/ncpv/images/efficiency_chart.jpg.

22. H. Liu, Z. Huang, S. Wei, L. Zheng, L. Xiao and Q. Gong, *Nanoscale*, 2016, **8**, 6209-6221.

23. Z. Yu and L. Sun, *Adv. Energy Mater.*, 2015, **5**, 1500213.

24. W. Ke, G. Fang, J. Wan, H. Tao, Q. Liu, L. Xiong, P. Qin, J. Wang, H. Lei, G. Yang, M. Qin, X. Zhao and Y. Yan, *Nat. Commun.*, 2015, **6**, 6700.

25. T. Zhang, M. Yang, Y. Zhao and K. Zhu, *Nano Lett.*, 2015, **15**, 3959-3963.

26. M. Yang, Y. Zhou, Y. Zeng, C. S. Jiang, N. P. Padture and K. Zhu, *Adv. Mater.*, 2015, **27**, 6363-6370.

27. D. Liu and T. L. Kelly, *Nat. Photo.*, 2013, **8**, 133-138.

28. B. Wang, K. Young Wong, X. Xiao and T. Chen, *Sci. Rep.*, 2015, **5**, 10557.

29. W. Ke, G. Fang, Q. Liu, L. Xiong, P. Qin, H. Tao, J. Wang, H. Lei, B. Li and J. Wan, *J. Am. Chem. Soc.*, 2015, **137**, 6730-6733.

30. W. Ke, D. Zhao, A. J. Cimaroli, C. R. Grice, P. Qin, Q. Liu, L. Xiong, Y. Yan and G. Fang, *J. Mater. Chem. A*, 2015, **3**, 24163-24168.

31. J. P. Correa Baena, L. Steier, W. Tress, M. Saliba, S. Neutzner, T. Matsui, F. Giordano, T. J. Jacobsson, A. R. Srimath Kandada, S. M. Zakeeruddin, A. Petrozza, A. Abate, M. K. Nazeeruddin, M. Grätzel and A. Hagfeldt, *Energy Environ. Sci.*, 2015, **8**, 2928-2934.

32. S. Albrecht, M. Saliba, J. P. Correa Baena, F. Lang, L. Kegelmann, M. Mews, L. Steier, A. Abate, J. Rappich, L. Korte, R. Schlatmann, M. K. Nazeeruddin, A. Hagfeldt, M. Grätzel and B. Rech, *Energy Environ. Sci.*, 2016, **9**, 81-88.

33. Y. Li, J. Zhu, Y. Huang, F. Liu, M. Lv, S. Chen, L. Hu, J. Tang, J. Yao and S. Dai, *RSC Adv.*, 2015, **5**, 28424-28429.

34. J. Song, E. Zheng, J. Bian, X.-F. Wang, W. Tian, Y. Sanehira and T. Miyasaka, *J. Mater. Chem. A*, 2015, **3**, 10837-10844.

35. Q. Dong, Y. Shi, K. Wang, Y. Li, S. Wang, H. Zhang, Y. Xing, Y. Du, X. Bai and T. Ma, *J. Phys. Chem. C*, 2015, **119**, 10212-10217.

36. H.-S. Rao, B.-X. Chen, W.-G. Li, Y.-F. Xu, H.-Y. Chen, D.-B. Kuang and C.-Y. Su, *Adv. Funct. Mater.*, 2015, **25**, 7200-7207.

37. C.-C. Chueh, C.-Z. Li and A. K. Y. Jen, *Energy Environ. Sci.*, 2015, **8**, 1160-1189.

38. W. Ke, C. Xiao, C. Wang, B. Saparov, H. S. Duan, D. Zhao, Z. Xiao, P. Schulz, S. P. Harvey, W. Liao, W. Meng, Y. Yu, A. J. Cimaroli, C. S. Jiang, K. Zhu, M. Al-Jassim, G. Fang, D. B. Mitzi and Y. Yan, *Adv. Mater.*, 2016, **28**, 5214–5221.

39. J. Shi, X. Xu, D. Li and Q. Meng, *Small*, 2015, **11**, 2472–2486.

40. G. Li, V. Shrotriya, J. Huang, Y. Yao, T. Moriarty, K. Emery and Y. Yang, *Nat. Mater.*, 2005, **4**, 864-868.

41. G. Li, R. Zhu and Y. Yang, *Nat. Photo.*, 2012, **6**, 153-161.

42. K. Wojciechowski, T. Leijtens, S. Spirova, C. Schlueter, M. Hoerantner, J. T.-W. Wang, C.-Z. Li, A. K.-Y. Jen, T.-L. Lee and H. J. Snaith, *J. Phys. Chem. Lett.*, 2015.

43. S. Ryu, J. Seo, S. S. Shin, Y. C. Kim, N. J. Jeon, J. H. Noh and S. I. Seok, *J. Mater. Chem. A*, 2015, **3**, 3271-3275.

44. W. Ke, D. Zhao, C. R. Grice, A. J. Cimaroli, J. Ge, H. Tao, H. Lei, G. Fang and Y. Yan, *J. Mater. Chem. A*, 2015, **3**, 17971-17976.

45. W. Ke, D. Zhao, C. R. Grice, A. J. Cimaroli, G. Fang and Y. Yan, *J. Mater. Chem. A*, 2015, **3**, 23888-23894.

46. Y. Deng, E. Peng, Y. Shao, Z. Xiao, Q. Dong and J. Huang, *Energy Environ. Sci.*, 2015, **8**, 1544-1550.

47. C. Bi, Y. Yuan, Y. Fang and J. Huang, *Adv. Energy Mater.*, 2014, **4**, 1401616.

48. D. Zhao, M. Sexton, H.-Y. Park, G. Baure, J. C. Nino and F. So, *Adv. Energy Mater.* , 2014, **5**, 1401855.

49. Y. Shao, Z. Xiao, C. Bi, Y. Yuan and J. Huang, *Nat. Commun.*, 2014, **5**, 5784.

50. C. Sun, Z. Wu, H.-L. Yip, H. Zhang, X.-F. Jiang, Q. Xue, Z. Hu, Z. Hu, Y. Shen, M. Wang, F. Huang and Y. Cao, *Adv. Energy Mater.* , 2016, **6**, 1501534.

51. P.-W. Liang, C.-C. Chueh, S. T. Williams and A. K. Y. Jen, *Adv. Energy Mater.*, 2015, **5**, 1402321.

52. C. Liu, K. Wang, P. Du, T. Meng, X. Yu, S. Z. Cheng and X. Gong, *ACS Appl. Mater. Interfaces*, 2015, **7**, 1153-1159.

53. J. Kim, G. Kim, T. K. Kim, S. Kwon, H. Back, J. Lee, S. H. Lee, H. Kang and K. Lee, *J. Mater. Chem. A*, 2014, **2**, 17291-17296.

54. C. Tao, S. Neutzner, L. Colella, S. Marras, A. R. Srimath Kandada, M. Gandini, M. D. Bastiani, G. Pace, L. Manna, M. Caironi, C. Bertarelli and A. Petrozza, *Energy Environ. Sci.*, 2015, **8**, 2365-2370.

55. A. Abrusci, S. D. Stranks, P. Docampo, H. L. Yip, A. K. Jen and H. J. Snaith, *Nano Lett.*, 2013, **13**, 3124-3128.

56. K. Wojciechowski, S. D. Stranks, A. Abate, G. Sadoughi, A. Sadhanala, N. Kopidakis, G. Rumbles, C.-Z. Li, R. H. Friend and A. K.-Y. Jen, *ACS nano*, 2014, **8**, 12701–12709.

57. Y. Li, Y. Zhao, Q. Chen, Y. M. Yang, Y. Liu, Z. Hong, Z. Liu, Y. T. Hsieh, L.

Meng, Y. Li and Y. Yang, *J. Am. Chem. Soc.*, 2015, **137**, 15540-15547.

58. X. Liu, K.-W. Tsai, Z. Zhu, Y. Sun, C.-C. Chueh and A. K. Y. Jen, *Adv. Mater. Interfaces*, 2016, **3**, 1600122.

59. N. Ahn, D. Y. Son, I. H. Jang, S. M. Kang, M. Choi and N. G. Park, *J. Am. Chem. Soc.*, 2015, **137**, 8696-8699.

60. H. J. Snaith, A. Abate, J. M. Ball, G. E. Eperon, T. Leijtens, N. K. Noel, S. D. Stranks, J. T.-W. Wang, K. Wojciechowski and W. Zhang, *J. Phys. Chem. Lett.*, 2014, **5**, 1511-1515.

61. S. van Reenen, M. Kemerink and H. J. Snaith, *J. Phys. Chem. Lett.*, 2015, **6**, 3808-3814.

62. W. Tress, N. Marinova, T. Moehl, S. M. Zakeeruddin, M. K. Nazeeruddin and M. Grätzel, *Energy Environ. Sci.*, 2015, **8**, 995-1004.

63. A. R. Pascoe, N. W. Duffy, A. D. Scully, F. Huang and Y.-B. Cheng, *J. Phys. Chem. C*, 2015, **119**, 4444-4453.

64. W. Ke, G. Fang, J. Wang, P. Qin, H. Tao, H. Lei, Q. Liu, X. Dai and X. Zhao, *ACS Appl. Mater. Interfaces*, 2014, **6**, 15959-15965.

65. A. Dualeh, T. Moehl, N. Tétreault, J. Teuscher, P. Gao, M. K. Nazeeruddin and M. Grätzel, *ACS Nano*, 2013, **8**, 362-373.

66. E. J. Juarez-Perez, M. Wubetaler, F. Fabregat-Santiago, K. Lakus-Wollny, E. Mankel, T. Mayer, W. Jaegermann and I. Mora-Sero, *J. Phys. Chem. Lett.*, 2014, **5**, 680-685.

67. A. K. Chandiran, A. Yella, M. T. Mayer, P. Gao, M. K. Nazeeruddin and M. Gratzel, *Adv. Mater.*, 2014, **26**, 4309-4312.

68. K. Wang, Y. Shi, B. Li, L. Zhao, W. Wang, X. Wang, X. Bai, S. Wang, C. Hao and T. Ma, *Adv. Mater.*, 2016, **28**, 1891-1897.

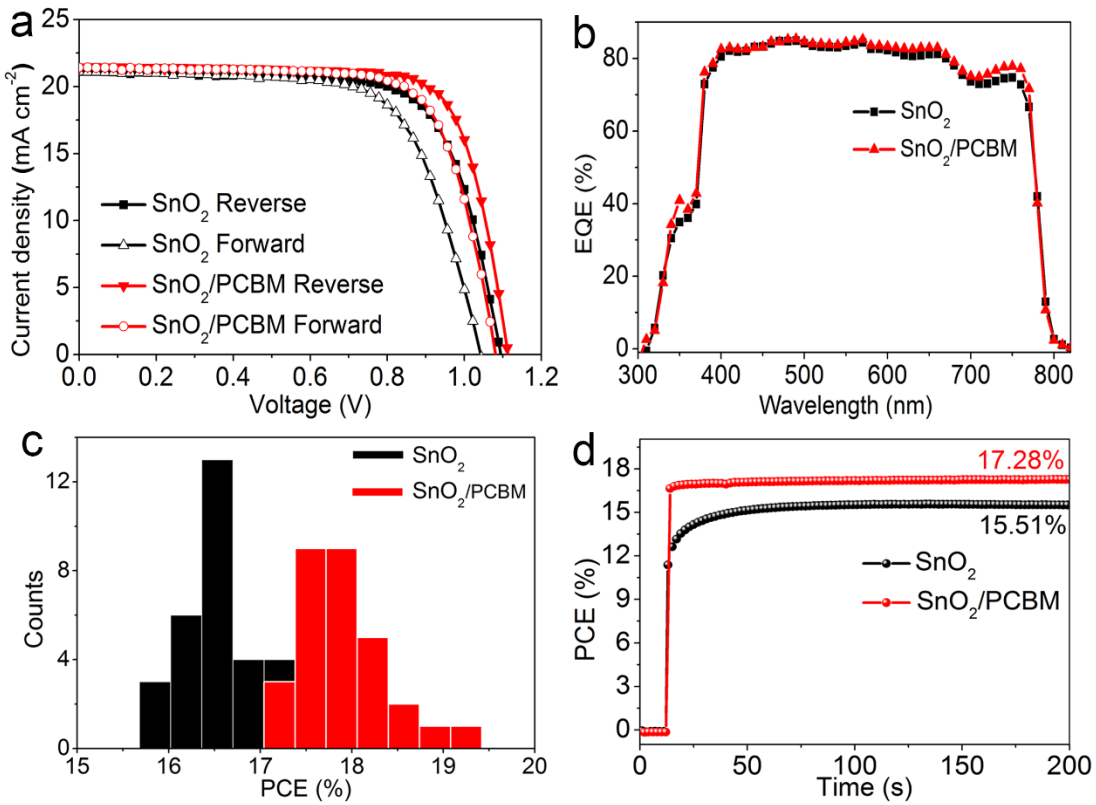

Fig. 1 (a) *J-V* curves of the perovskite solar cells using SnO_2 and SnO_2/PCBM ESLs under reverse and forward voltage scanning. (b) EQE spectra of the cells using SnO_2 and SnO_2/PCBM ESLs. (c) Histograms of PCEs for 30 cells with SnO_2 ESLs and 30 cells with SnO_2/PCBM ESLs measured under reverse voltage scanning. (d) Steady-state efficiencies of the cells using SnO_2 and SnO_2/PCBM ESLs at constant bias voltages of 0.889 V and 0.911 V, respectively.

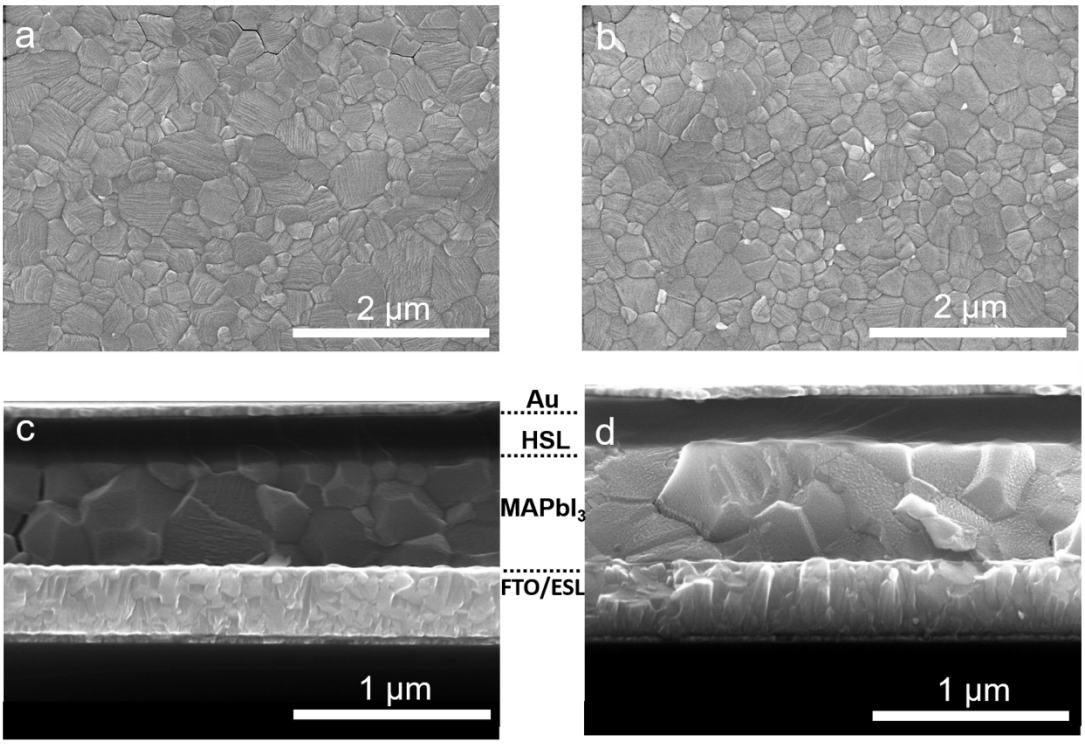

Fig. 2 Top view SEM images of perovskite films deposited on (a) SnO_2 ESL and (b) SnO_2/PCBM ESL. Cross-sectional SEM images of completed devices using (c) SnO_2 ESL and (d) SnO_2/PCBM ESL.

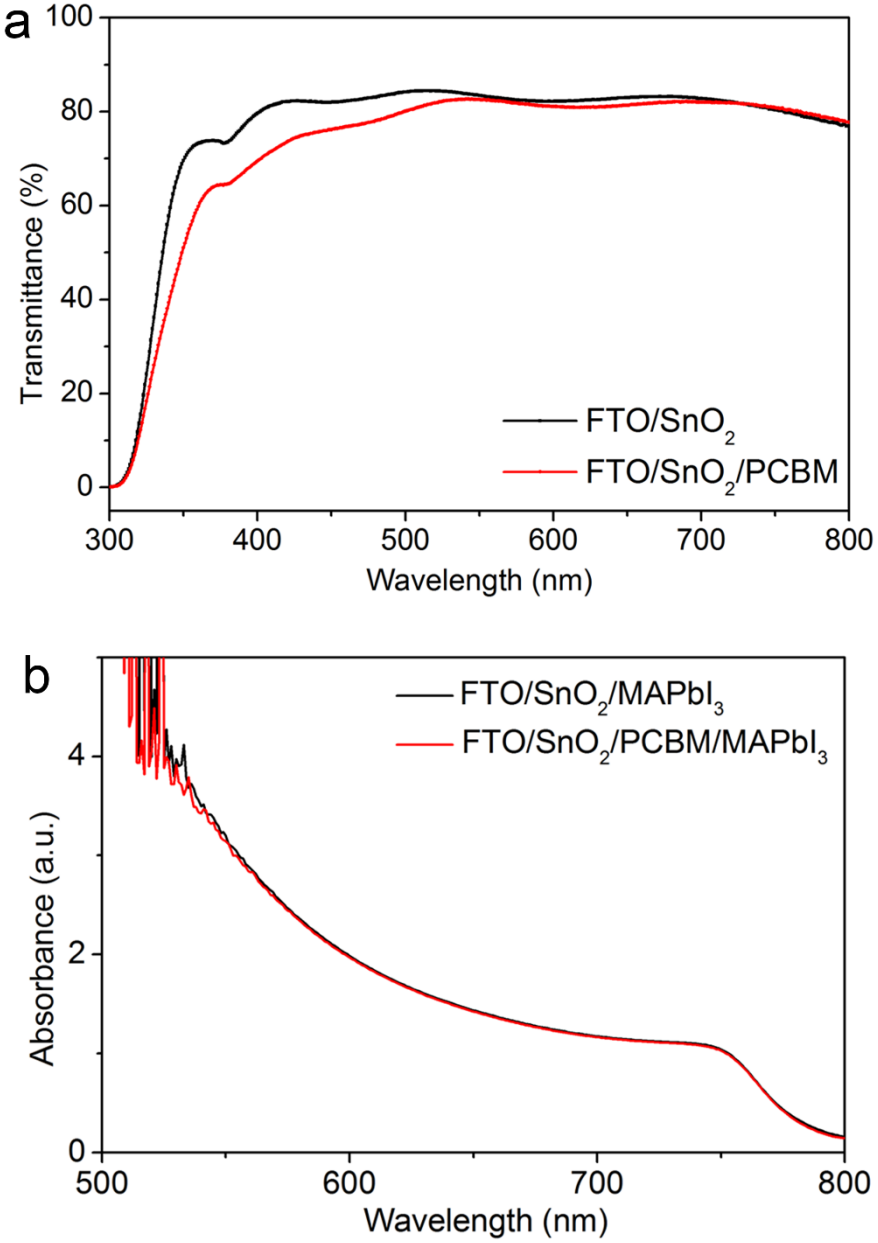

Fig. 3 (a) Transmission spectra of FTO substrates coated with SnO_2 and SnO_2/PCBM. (b) UV-vis absorbance spectra of perovskite films grown on SnO_2 and SnO_2/PCBM ESLs.

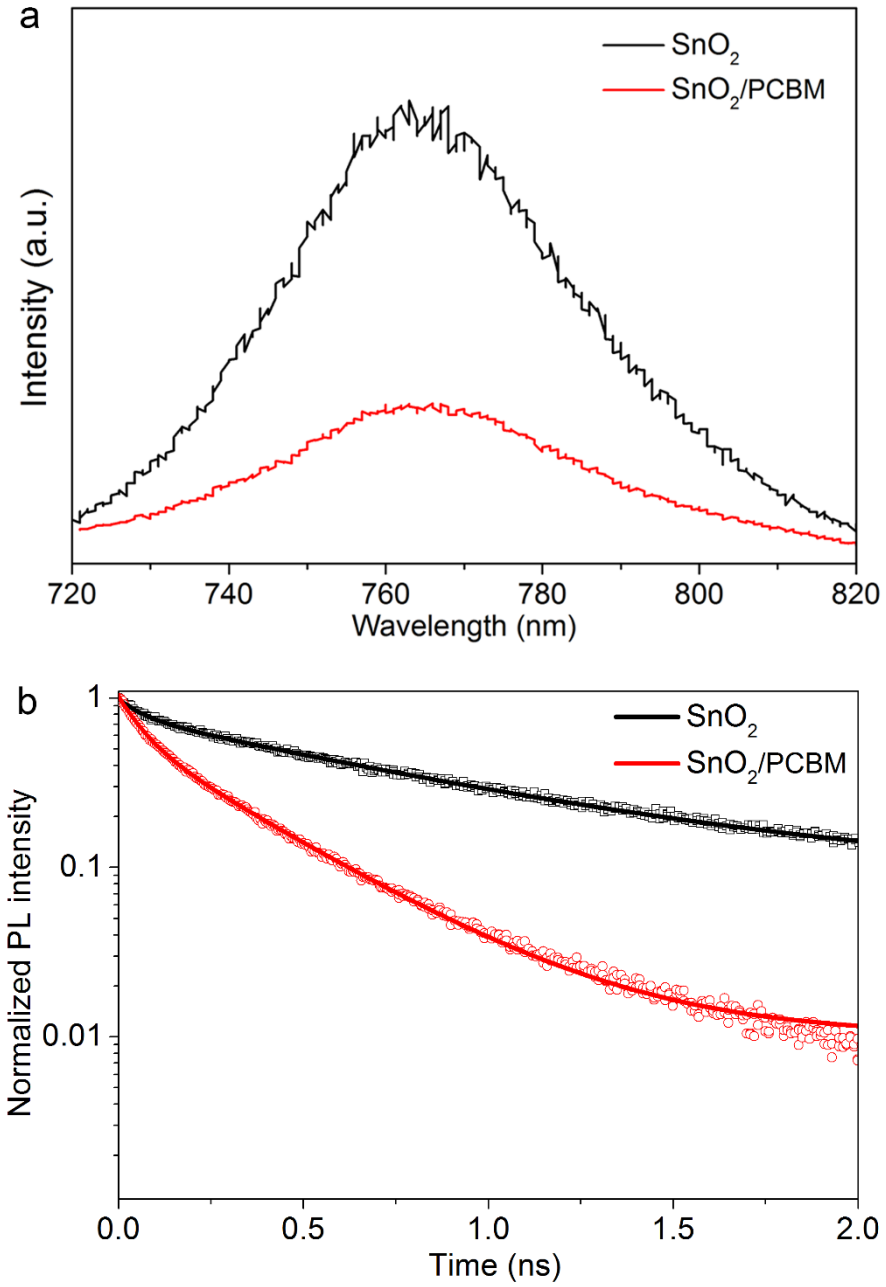

Fig. 4 (a) PL spectra and (b) TRPL decay transient spectra of perovskite films deposited on SnO_2 and SnO_2/PCBM ESLs.

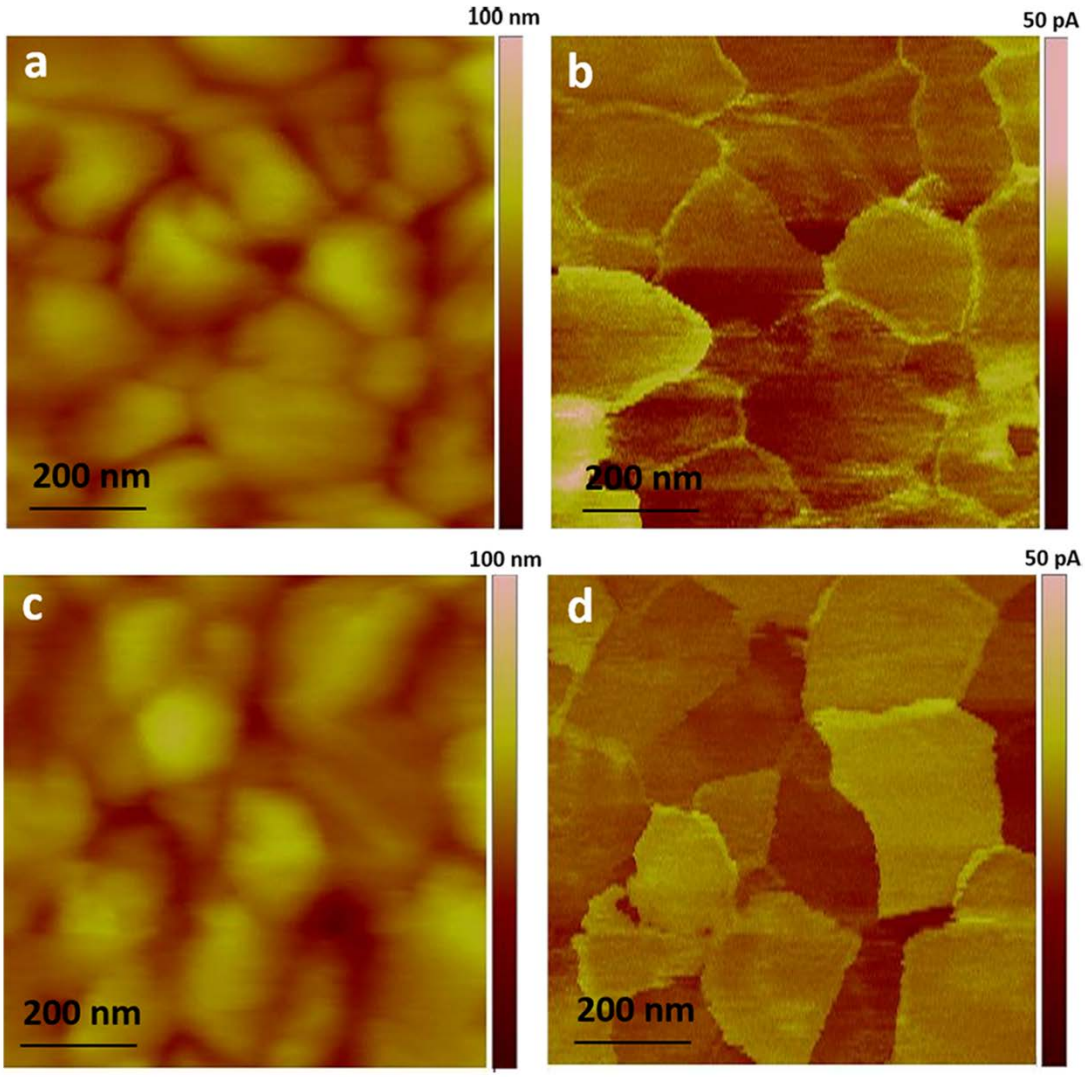

Fig. 5 AFM and the corresponding c-AFM images of the perovskite films deposited on (a, b) SnO_2 and (c, d) SnO_2/PCBM ESLs.

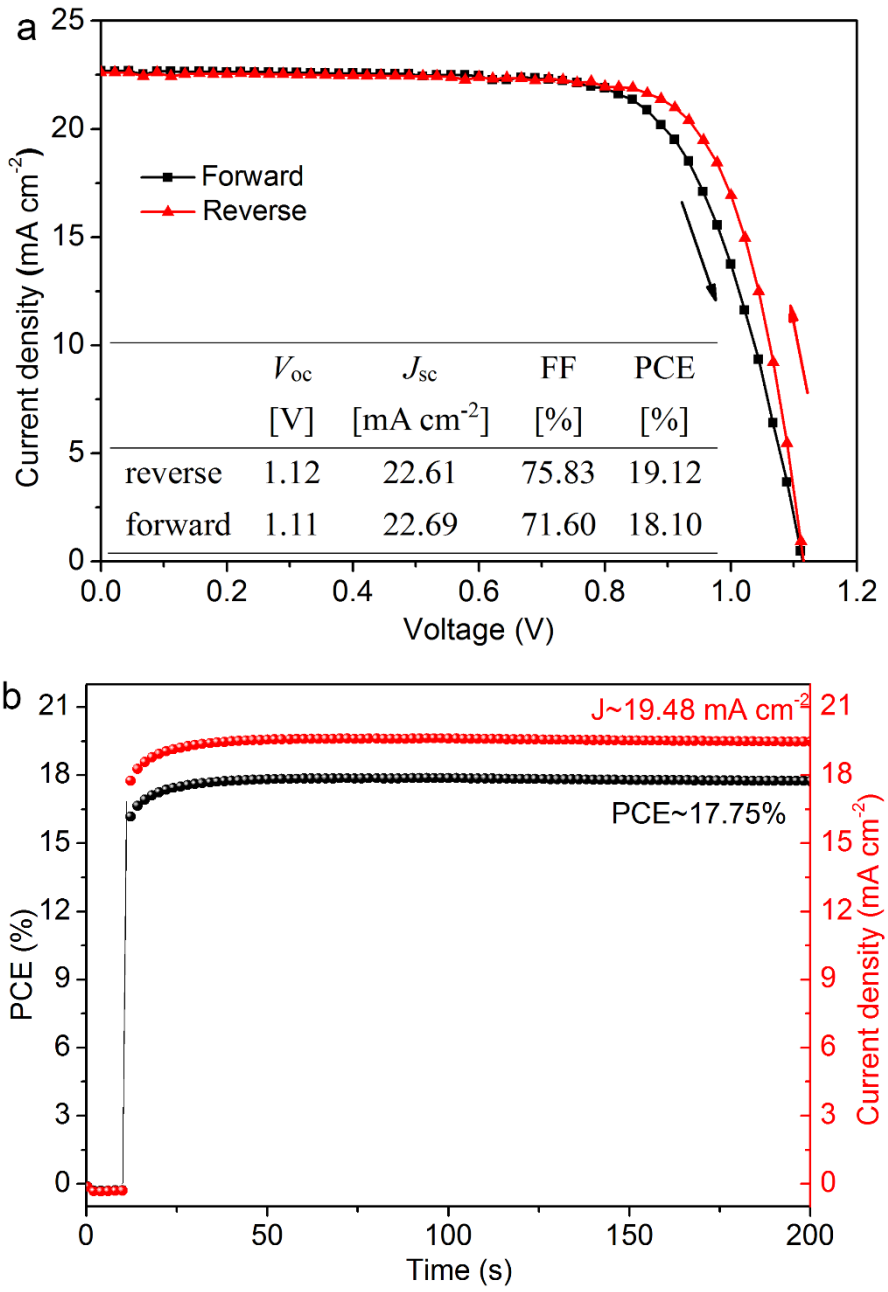

Fig. 6 (a) *J-V* curves of the best-performing perovskite solar cell using SnO_2/PCBM ESL measured under reverse and forward voltage scanning. (b) Steady-state efficiency of the best-performing cell using SnO_2/PCBM ESL at a constant bias voltage of 0.911 V.

Table 1 Summary of photovoltaic parameters of the cells using SnO_2 and SnO2/PCBM ESLs measured under reverse and forward voltage scanning.

	V_{oc} [V]	J_{sc} [mA cm^{-2}]	FF [%]	PCE [%]
SnO_2 (reverse)	1.09	21.13	71.49	16.53
SnO_2 (forward)	1.04	21.10	67.77	14.91
SnO_2/PCBM (reverse)	1.11	21.41	76.20	18.17
SnO_2/PCBM (forward)	1.08	21.42	73.01	16.91

Table of Contents

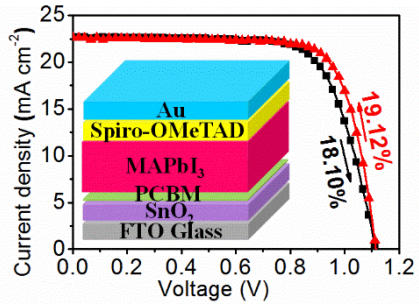

Fullerene passivated tin oxide electron selective layers enhance the performance of planar perovskite solar cells